Nuclear Science and Techniques (2023) 34:183
https://doi.org/10.1007/s41365-023-01324-x

Spatial and spectral measurement of laser-driven protons through radioactivation

Yin-Ren Shou[1] · Xue-Zhi Wu[1,2] · Gwang-Eun Ahn[1] · Seung Yeon Kim[1] · Seong Hoon Kim[3] · Hwang Woon Lee[1] · Jin Woo Yoon[1,3] · Jae Hee Sung[1,3] · Seong Ku Lee[1,3] · Xue-Qing Yan[2] · Il Woo Choi[1,3] · Chang Hee Nam[1,4]

Received: 4 June 2023 / Revised: 19 July 2023 / Accepted: 20 July 2023 / Published online: 30 November 2023

Abstract
The simultaneous measurement of the spatial profile and spectrum of laser-accelerated protons is important for further optimization of the beam qualities and applications. We report a detailed study regarding the underlying physics and regular procedure of such a measurement through the radioactivation of a stack composed of aluminum, copper, and CR-39 plates as well as radiochromic films (RCFs). After being radioactivated, the copper plates are placed on imaging plates (IPs) to detect the positrons emitted by the reaction products through contact imaging. The spectrum and energy-dependent spatial profile of the protons are then obtained from the IPs and confirmed by the measured ones from the RCFs and CR-39 plates. We also discuss the detection range, influence of electrons, radiation safety, and spatial resolution of this measurement. Finally, insights regarding the extension of the current method to online measurements and dynamic proton imaging are also provided.

Keywords Laser-driven proton acceleration · Proton-induced nuclear reaction · Radioactivation measurement · Contact imaging

1 Introduction

Laser-accelerated proton beams, with the advantages of having a picosecond-scale duration, ultrahigh brightness, and micrometer source size [1], are promising for various applications [2] including transient dynamics detection [3], bi-modal radiographic imaging [4], and FLASH radiotherapy [5, 6]. For instance, laser-accelerated protons have been directly applied in FLASH irradiation on cells with an ultrahigh dose rate of 10^9 Gy/s [7]. In addition, manipulation of the proton beam using a tunable active plasma lens [8] or a pulsed two-solenoid beamline [9] has been demonstrated, indicating the feasibility of delivering tailored dose distributions. A more accurate control of protons with an image-relaying beam line has been reported as well, demonstrating a stable production of proton beams with a tunable energy and energy spread <1% [10]. Understanding the underlying physics of laser-driven proton acceleration and realizing a better manipulation of accelerated protons according to requirements entail the spatial and spectral measurement of laser-accelerated protons. This is challenging for conventional diagnostic tools [11] owing to the ultrashort beam

This work was supported by the Institute for Basic Science, Korea under the project code IBS-R012-D1 and by the Ultrashort Quantum Beam Facility (UQBF) operation program (No. 140011) through APRI, GIST.

✉ Il Woo Choi
iwchoi@gist.ac.kr

✉ Chang Hee Nam
chnam@gist.ac.kr

[1] Center for Relativistic Laser Science, Institute for Basic Science, Gwangju 61005, Republic of Korea

[2] School of Physics, Peking University, Beijing 100871, China

[3] Advanced Photonics Research Institute, Gwangju Institute of Science and Technology, Gwangju 61005, Republic of Korea

[4] Department of Physics and Photon Science, Gwangju Institute of Science and Technology, Gwangju 61005, Republic of Korea

duration, simultaneous generation of multi-species ions [12] and X-rays [13–15] as well as hostile environments such as the occurrence of intense electromagnetic pulses during laser-driven proton acceleration [16, 17].

Several types of detectors have been used to characterize laser-accelerated protons, the most common being the Thomson parabola spectrometer (TPS), which has a high energy resolution and can be utilized online if a microchannel plate (MCP) [18, 19] or a scintillator [20] is applied to record the ion trajectories. However, TPS, as well as another type of real-time detector using the time-of-flight technique [21], cannot obtain the spatial information of protons owing to their significantly small detection angle. A modified design of TPS using a multi-pinhole array instead of a single pinhole can extend the spatial resolution to several different directions [22–24]. Additionally, an angular spectrometer using only a magnetic field and replacing the pinhole with a narrow slit [25, 26] or a two-dimensional (2D) pinhole array [27] has been utilized to obtain the 1D or 2D profile of ions, although the capability of distinguishing different ion species is significantly limited. A stack spectrometer has been widely applied to obtain an accurate 2D profile of laser-accelerated protons; however, this is at the expense of the energy resolution. These stacks can consist of scintillator, imaging plate (IP), radiochromic film (RCF), nuclear track detector, and absorption layer. Among these, only the scintillator-based stack can be utilized online with the help of cameras [28]. To resolve the proton spectrum from the scintillation signals, various solutions have been demonstrated, including placing absorbers with different thicknesses before a scintillator [29–32], imaging the layer edge of each scintillator in the stack for a 1D spatial measurement [33], and distinguishing the signals from different layers of scintillators through their varying relative angles [34] or central wavelengths [35]. The main disadvantage of a scintillator is its relatively low sensitivity and spatial resolution. While IP [36] and RCF [37] can provide a higher resolution, both are sensitive to electrons that intrinsically exist during laser-driven proton acceleration and can induce significant noise. A nuclear track detector, such as the Columbia Resin #39 (CR-39) [38], is insensitive to electrons and has the highest spatial resolution. Hence, the use of CR-39 is regarded as the most robust measurement method, although its low saturation fluence and complex etching process limit its widespread application [39]. Another robust method is the radioactivation measurement based on proton-induced nuclear activation in the absorption layers with an activation material, which was also applied in previous experiments [40, 41].

In practice, the radioactivation measurement usually involves two steps. First, nuclei in the absorption layers capture energetic protons and produce isotopes (mainly β^+ emitters); second, the activity of each absorption layer is measured by coincidence detection, gamma-ray spectrometry, or contact imaging. Among these, coincidence detection was first introduced in the field of laser-driven proton acceleration [42, 43]. The activity is measured by counting the 511-keV annihilation gamma rays using coincidence detectors; radioactive isotopes are identified by measuring the half-life [44, 45]. Improved isotope identification can be achieved by gamma-ray spectrometry, in which nuclides and corresponding reactions are distinguished by the emitted characteristic gamma rays [46]. Following the activity measurement, the proton spectrum can be derived considering the cross-section of the activation and the Bragg peak energy of each absorption layer. To further obtain the spatial information of protons, contact imaging (autoradiography) was developed by exposing the activated layers onto IPs [47] and has been demonstrated in several experiments with the spatial and spectral reconstruction of the protons [48, 49]. However, in these studies, the signals on the IPs were attributed to gamma rays from the activated layers; a comprehensive study regarding contact imaging has not been reported thus far, which limits its wide application in laser-accelerated proton characterization.

In this study, we provide a detailed discussion regarding the underlying physics and regular procedure of contact imaging for the spatial and spectral measurement of laser-driven protons through radioactivation. A stack composed of aluminum, copper, and CR-39 plates as well as RCFs was designed and radioactivated by protons with a cutoff energy exceeding 50 MeV driven by a petawatt laser. After being radioactivated, the copper plates were placed on IPs for contact imaging. The energy-dependent spatial profiles of the protons were then directly obtained from the IPs and validated by the measured ones with the RCFs and CR-39 plates. The proton spectrum was also derived based on the nuclear reaction possibility and average response of each copper plate calculated from the Monte Carlo (MC) code FLUKA [50], which sufficiently matched the results measured using RCF and CR-39. The MC simulation indicated that the signals of the IPs were mainly from the positrons, instead of the gamma rays, in activated layers. Furthermore, the detectable proton fluence, the influence of electrons, and the spatial resolution were also discussed, demonstrating the advantage and robustness of this method. Finally, insights regarding the extension of the current method to online measurements and dynamic proton imaging are presented.

2 Experiments

The petawatt laser at the Center for Relativistic Laser Science (CoReLS) was utilized to accelerate the protons and demonstrate a spatial and spectral measurement through radioactivation. A simple schematic of the experimental

layout is displayed in Fig. 1. A linearly polarized laser pulse was focused onto a 52-nm-thick polymer (F8BT, $C_{35}H_{42}N_2S$) target at an incident angle of 33° using an f/3.6 off-axis parabolic mirror (OAP). A double plasma mirror system was applied to ensure that the laser contrast was sufficiently high for such ultrathin targets [51]. The duration, on-target energy, spot-size in full width at half maximum (FWHM), and energy concentration in FWHM area of the laser were 26 fs, 20 J, 3.2 μm, and 30%, respectively, corresponding to a peak intensity of 3×10^{21} W/cm^2. Ultrashort protons with an exponentially decaying spectrum and a cut-off energy exceeding 50 MeV can be accelerated from the rear surface of the target.

A stack was designed as listed in Table 1 and applied in the experiment to measure the spatial profile and spectrum of the accelerated protons. All layers had the same transverse size of 5 cm × 5 cm. The first 0.5-mm-thick aluminum plate was assembled to block visible light and carbon ions below 190 MeV [52]; behind it, ten pieces of RCFs (Gafchromic) were utilized with a 5-MeV energy gap between the Bragg peaks of protons, as shown in the curves of deposited energy in Fig. 2. The first four RCFs were HD-V2 type (dynamic range 10–1000 Gy), whereas the last six were EBT-3 type (dynamic range 0.1–20 Gy) considering the relatively low number of the high-energy protons [53]. The radioactivation measurement was achieved by four copper plates, of which the last two had a larger thickness owing to the lower proton number in the high energy region. We also inserted five pieces of CR-39 (Track Analysis Systems Ltd.) in the stack to validate the results from the radioactivation measurement.

During the experiment, an online TPS was first utilized to determine the optimal conditions of the laser and target.

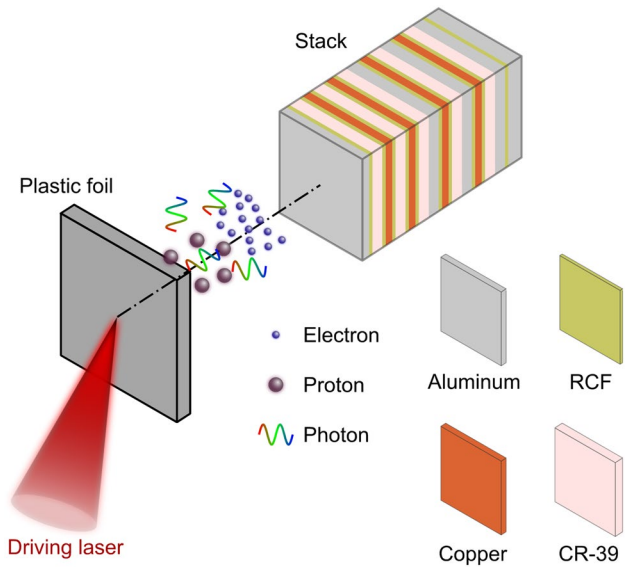

Fig. 1 (Color online) Schematic of the experimental layout

Table 1 Composition of the stack used in this study. HD and EBT refer to HD-V2 and EBT3 type RCFs, respectively

Layer #	Material	Layer #	Material	Layer #	Material
1	0.5-mm Al	9	0.3-mm Cu	17	1.0-mm Al
2	HD-1	10	EBT-1	18	EBT-4
3	CR-39	11	CR-39	19	0.5-mm Cu
4	HD-2	12	1.0-mm Al	20	EBT-5
5	0.3-mm Cu	13	EBT-2	21	CR-39
6	HD-3	14	0.5-mm Cu	22	1.5-mm Al
7	CR-39	15	EBT-3	23	EBT-6
8	HD-4	16	CR-39	24	2.0-mm Al

Subsequently, the prepared stack, which was installed on a linear stage, was moved in and placed 15 mm from the rear surface of the target to the first layer. After one laser shot, the stack was moved into a small chamber for a quick exchange [54]; the copper plates in the stack were then placed on the surface of a BAS-MS imaging plate (Fujifilm) for exposure. The use of an exchange chamber can reduce the time interval between the end of laser shot and the start of exposure to only 18 min, which is important for the detection of ^{62}Cu as this product has a short half-life of 9.672 min. After a 20-min exposure, the IP was quickly sent to a scanner (Amersham Typhoon). During this process, the IP was shielded with an aluminum foil to avoid the influence of visible light. The scan parameters included a resolution of 100 μm, dynamic range of $L = 5$, and sensitivity of $S = 4000$.

To validate the spatial profile and spectrum of protons obtained from the radioactivation method, we also processed

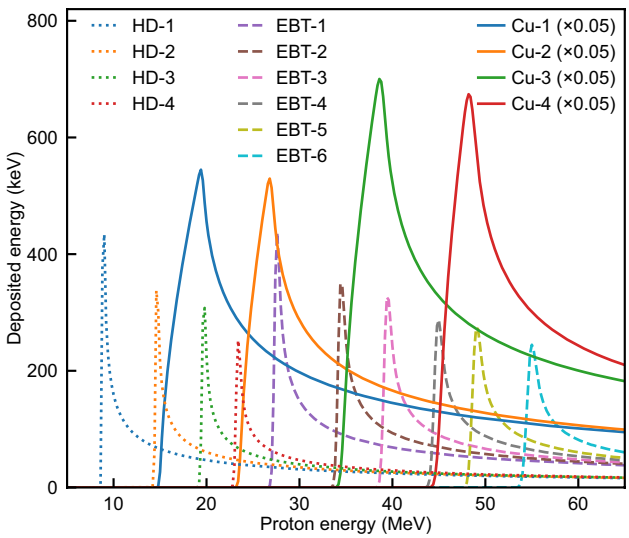

Fig. 2 (Color online) Deposited energy of each layer in the stack depending on the initial incident proton energy on the stack. A scale factor of 0.05 was applied for the data of the copper plates (solid lines)

the RCF and CR-39 in the stack. After waiting longer than 24 h to ensure the stabilization of the irradiated RCF, we scanned it using a 48-bit color scanner (Epson Perfection V750 Pro) in transmission mode at a resolution of 300 dots per inch (dpi) with no color correction [55]. Unexposed RCFs and a black aluminum foil were scanned with the same setting as the reference and the background, respectively. The CR-39 was first etched in a 6.25 N NaOH solution at a constant temperature of 70 °C for 4 h to visualize the latent track [56]. After etching, the CR-39 was cleaned and scanned using an upright microscope (Olympus BX53M) under a magnification of 25× to record the pits on the front and rear surfaces. Owing to the limit that each frame of the microscope had an imaging area of only 251 μm × 141 μm, thousands of frames were recorded and automatically joined to count the pits.

3 Results

The spatial profile of the laser-accelerated protons, which can provide a better understanding of the acceleration mechanism, can be directly obtained from the scanned IPs after contact imaging by the radioactivated copper plates. Figure 3e–h displays the source data of the IPs corresponding to the four copper plates with Bragg peak energies of approximately 20, 30, 40 and 50 MeV, as shown in Fig. 2. The center of the proton beam deflects only several degrees from the normal direction of the target toward the laser propagation direction, and the beam divergence decreases as the proton energy E_p increases when $E_p > 0.2E_c$, where E_c is the cutoff energy, indicating that the protons were mainly accelerated by target normal sheath acceleration (TNSA) rather than by radiation pressure acceleration (RPA) [11]. The spatial profile measured through radioactivation was validated by the results from each RCF placed just behind the copper plate in the stack, as depicted in Fig. 3a–d. Apparent noise from the electrons, as shown in the left part of Fig. 3b in comparison with Fig. 3f, and a structure of protons in the central part reveal the robustness and high dynamic range of the radioactivation method.

The spatial profile from CR-39 sufficiently agrees with that from the radioactivation measurement and RCF, as shown in Fig. 3d, h, and i. Here, only the last CR-39 was processed because the others were significantly overexposed owing to the low saturation fluence of approximately 10^7 protons/cm^2 [39]. For a quantitative analysis, an ImageJ [57] script was developed to count the diameters of the etched pits on the front and rear surfaces of CR-39. Corresponding to different etching stages, these pits can be divided into conical (dark circle) and spherical (dark donut with a brighter center) phases [58] according to their profiles. The incident energy of a proton can be deduced from the phases

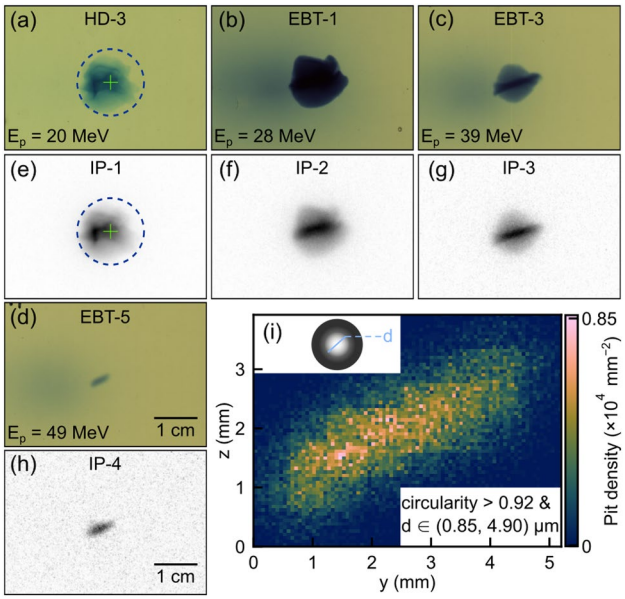

Fig. 3 (Color online) Energy-dependent spatial profiles of protons measured through RCF (a–d), radioactivation (e–h), and CR-39 (i). The cross in (a) indicates the normal direction to the rear surface of the target, while the dashed circle corresponds to the full divergence angle of 25°. In the inset of (i), the sketch of a typical proton pit in the spherical phase [58] on the front surface of CR-39 is provided. Only pits with a circularity of larger than 0.92, and inner diameter d between 0.85 μm and 4.90 μm are counted in (i), corresponding to protons whose energies are below 0.7 MeV when reaching the front surface of the last CR-39 [59]

and diameters of the pits after considering the etching temperature and time. Here, we utilized the calibrated relationships between the pit diameter and proton energy for the front [59, 60] and rear surfaces [61] of CR-39. In Fig. 3i, the distribution of the pits caused by protons with initial incident energies of approximately 50 MeV is displayed, where both the size and slope of the spatial profile are consistent with those from the IP and RCF at a similar proton energy.

In addition to the energy-dependent spatial profiles, the proton spectrum can be simultaneously generated from the radioactivation measurement. For each copper plate, we can assume a spectral intensity S_i at its Bragg peak energy E_i; the logarithmic proton spectrum $\log[S(E)]$ can be simply obtained by the linear interpolation of $\log(S_i)$ accompanied with linear extrapolation. Then, the supposed yield of each nuclear reaction product j in the ith copper plate is $\int S(E)P_{ij}(E)\mathrm{d}E$, where $P_{ij}(E)$ is the energy-dependent possibility of the nuclear reaction product j in the ith plate. Table 2 lists the main channels of the proton-induced nuclear reactions in copper; the corresponding P_{ij} of these products were calculated by FLUKA simulations [50, 62] using the same setup of the proton beam and stack configuration as in the experiment. Considering the cross-section of the reaction and the half-life of the product, the main products are ^{62}Cu

and ^{63}Zn, whose P_{ij} are depicted in Fig. 4c. Subsequently, we performed another FLUKA simulation by simply placing an activated copper plate on an IP to calculate the mean deposited energy of one decaying nucleus, and further the mean photo-stimulated luminescence (PSL) value R_{ij} using the calibrated relationship of 0.75 ± 0.11 mPSL/keV [63, 64], as displayed in Fig. 4b. As a result, the assumed PSL value in the ith copper plate is as follows:

$$\mathrm{PSL}_i = \sum_j \int S(E) P_{ij}(E)(e^{-t_s/t_j} - e^{-t_e/t_j}) R_{ij} \mathrm{d}E. \quad (1)$$

Here, t_s (t_e) indicates the time interval between the start (end) of the exposure and the radioactivation, and t_j is related to the half-life of the product j as $t_j = T_{1/2}/\ln 2$. Finally, a differential evolution algorithm based on the Python package scikit-opt [65] is utilized to generate the measured proton spectrum $S(E)$ by fitting each assumed PSL value to the measured one through iterations of the values of S_i.

In practice, to obtain the measured PSL value of each plate, we first convert the count value in the source file using the following relationship:

$$\mathrm{PSL} = \left(\frac{4000}{S}\right)\left(\frac{R_{\mu m}}{100}\right)^2 10^{L(G/65535-1/2)}, \quad (2)$$

where the spatial resolution in μm unit is $R_{\mu m} = 100$, the dynamic range is $L = 5$, and the sensitivity is $S = 4000$ [66, 67]. Subsequently, the measured PSL_i is obtained, as shown in Fig. 4a, by summing all the PSL values in a copper plate, considering the corrections for the background noise and the time fading effect according to previous calibrations [66]. For the calculation of the fitted PSL_i, it should be noted that the responses R_{ij} of the main products ^{62}Cu and ^{63}Zn strongly depend on the thickness of the copper plate. Figure 4d shows the final proton spectrum obtained from a least-square fit of PSL_i to that of the measured one, as displayed in Fig. 4a. Here, a comprehensive uncertainty of 30% is used, which is determined by the fluctuation of the scanner sensitivity [67] and the uncertainty in the calibration of IPs [64].

We also calculated the proton spectrum from the ten RCFs using a similar procedure to validate the result from the radioactivation measurement. Here, the total deposited energy TDE_i in each RCF is utilized instead of the PSL value. The calculated TDE_i is also obtained from an

Table 2 Main proton-induced nuclear reactions in copper [71]. E_{th} and σ_m indicate the threshold proton energy and maximum cross-section of the reaction, respectively. $T_{1/2}$ is the half-life of the product

Reaction	E_{th} (MeV)	σ_m (barn)	Product	$T_{1/2}$
^{63}Cu(p,n)	4.2	0.5	^{63}Zn	38.47 m
^{63}Cu(p,n+p)	12	0.6	^{62}Cu	9.672 m
^{65}Cu(p,3n)	23	0.1	^{63}Zn	38.47 m
^{65}Cu(p,n)	2.2	0.8	^{65}Zn	243.9 d
^{63}Cu(p,2n)	13	0.1	^{62}Zn	9.193 h
^{65}Cu(p,n+p)	12	0.5	^{64}Cu	12.70 h
^{63}Cu(p,2n+p)	20	0.3	^{61}Cu	3.343 h

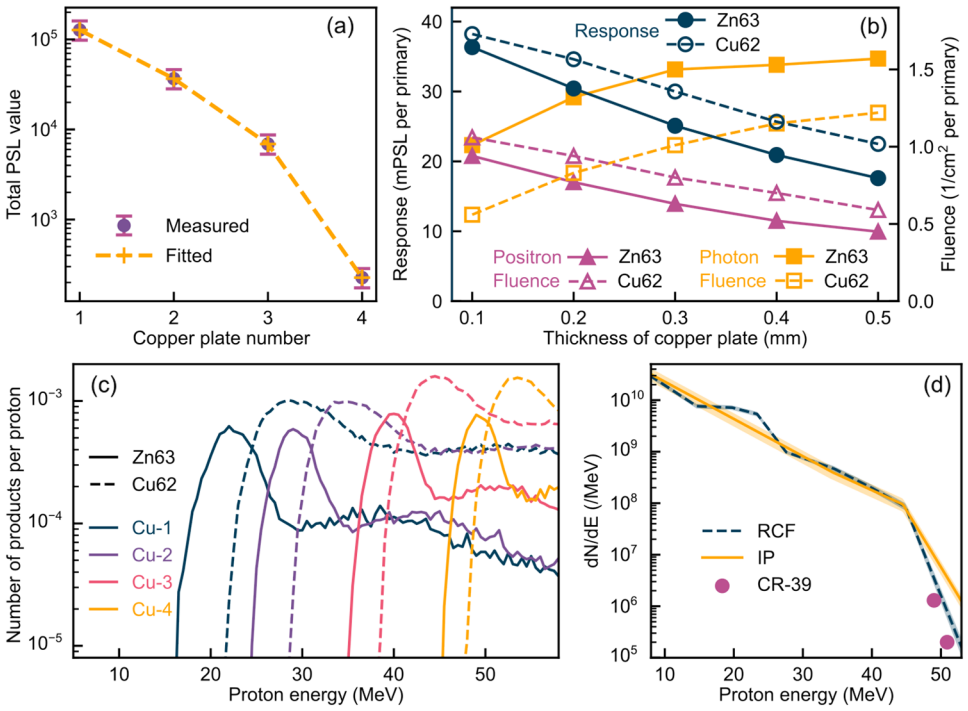

Fig. 4 (Color online) Proton spectrum unfolded from the radioactivation measurement. (a) Integral PSL value of each exposed IP. The vertical error bars represent the uncertainty of the scanner sensitivity. (b) Response R_{ij} as well as the fluence of the positrons and photons versus the copper plate thickness. (c) Normalized product yield $P_{ij}(E)$ as a function of the initial incident proton energy into the stack. (d) Proton spectra measured with the radioactivation on copper plates, RCF, and CR-39, respectively. The uncertainty of the spectra is indicated by the filled area

assumed spectrum $S(E)$ based on the spectral intensity S_i and the deposited energy curve D_i as:

$$\mathrm{TDE}_i = \int S(E) D_i(E) \mathrm{d}E, \tag{3}$$

where $D_i(E)$ is plotted in Fig. 2. For the measured TDE_i, we first converted the pixel value (PV) in the red channel of the scanned RCF to the optical density (OD) as follows:

$$\mathrm{OD}_i = \log_{10}\left(\frac{\mathrm{PV}_{\mathrm{un}} - \mathrm{PV}_{\mathrm{bg}}}{\mathrm{PV}_{\mathrm{ir}} - \mathrm{PV}_{\mathrm{bg}}}\right). \tag{4}$$

Here, $\mathrm{PV}_{\mathrm{un}}$ and $\mathrm{PV}_{\mathrm{ir}}$ are the PVs before and after the irradiation of the proton beam, respectively, while $\mathrm{PV}_{\mathrm{bg}}$ is the background of the scanner generated through scanning a black aluminum plate with the same size as the RCF [55]. Then, the measured TDE_i can be generated from the sum of the deposited energy in each pixel as follows:

$$\mathrm{TDE}_i = \sum m_{\mathrm{r}} f(\mathrm{OD}_i), \tag{5}$$

where m_{r} is the mass of the sensitive layer with the size of one pixel, which is determined by the scan resolution, and $f(OD)$ is the function between dose and OD value. Considering the scanner model, we utilized the $f(OD)$ of the HD-V2 and EBT-3 from previous calibration studies, [68] and [69, 70], respectively. By fitting the calculated TDE_i to that of the measured one, the proton spectrum was derived as indicated by the dashed line displayed in Fig. 4d. The spectra generated from both the radioactivation and RCF sufficiently agree, and the spectrum from the RCF has a finer shape because more pieces of RCFs were used.

The last CR-39 was also processed, and both of the spectral intensities $\mathrm{d}N/\mathrm{d}E$ from the front and rear surfaces were plotted, as shown in Fig. 4d, demonstrating a good consistency with the RCF spectrum. Here, we used the front surface as an example. First, the pits induced by the protons whose energies are below 0.7 MeV when they reach the front surface are counted. The total number is $\Delta N = 2.6 \times 10^4$ as shown in Fig. 3i. Then, the possibility distribution $P(E)$ of these protons, which is a function of the initial incident proton energy E into the stack, is calculated by FLUKA simulations. Finally the spectral intensity is $\mathrm{d}N/\mathrm{d}E = \Delta N / \int P(E)\mathrm{d}E$.

4 Discussion

To accurately unfold the spectrum of laser-accelerated protons through the radioactivation measurement, the average response of product j in the ith copper plate R_{ij} is important, which has not been clearly discussed in previous studies [47–49]. As indicated in the aforementioned sections, the main contributions during contact imaging on the IP are from the decay of ^{63}Zn and ^{62}Cu in the radioactivated plate. Both have a 100% β^+ decay branch [71], which indicates that the sensitive layer in the IP is exposed by the emitted positrons (broad spectrum, 0−2.2 MeV from ^{63}Zn and 0−2.9 MeV from ^{62}Cu), characteristic gamma rays (main lines of 670 keV and 962 keV from ^{63}Zn and of 1.17 MeV from ^{62}Cu), and gamma rays from the annihilation of positrons (511 keV). Considering that the thickness of the sensitive layer in the BAS-MS IP is only 115 μm [63], the energy deposited by a positron is approximately two orders of magnitude greater than that by a gamma-ray photon [72]. Hence, R_{ij} is mainly determined by the number of positrons reaching the sensitive layer. As the copper thickness increases, a larger fraction of positrons is annihilated inside the copper plate, leading to an increase of the photon fluence, as shown in Fig. 4b, while the R_{ij} decreases owing to the reduction of the positron fluence for thicker plates.

In our experiment, both the spatial profile and spectrum of protons measured through the radioactivation, RCF, and CR-39 sufficiently agree with one another. Compared to other methods, the radioactivation measurement mainly has the advantages of a high detection range (proton spectral intensity of $10^7 - 10^{12}$ MeV^{-1}) and good robustness to electron noise. CR-39 has a significantly low saturation fluence, rendering it only suitable for measuring the high-energy part of laser-driven protons, as displayed in Fig. 4d. For each specific type of RCF, its dose range is less than three orders of magnitude [53] owing to the nonlinear relationship between the OD value and dose [70]. Regarding the radioactivation measurement, the IP has a linear response of five orders of magnitude. The dynamic range can be further extended by a repeat of the scan [36], ensuring its ability to simultaneously image the center and edge parts of laser-accelerated proton beams. In the meantime, this imaging is accurate because the radioactivation method is less sensitive to electrons, which are accelerated along with the protons by the laser. These electrons usually propagate along the laser direction with a maximum energy of tens of MeV, which is sufficiently energetic to penetrate a 10-cm depth in water [73]. Hence, they can reach the last RCF in the stack and introduce significant noise, as shown in the left part of Fig. 5a. The electron noise has a similar strength compared to the proton signal, as depicted in Fig. 5c, strongly influencing the measurement of the proton beam profile, which can be worse for a normal incident laser in which the electron and proton overlap. In the result obtained through radioactivation, as displayed in Fig. 5b and c, there is no apparent noise from the electrons owing to the small cross-sections of the electron-induced nuclear reactions in the copper plate. Bremsstrahlung gamma rays induced by the electrons may trigger photonuclear reactions, such as $^{63}\mathrm{Cu}(\gamma, \mathrm{n})^{62}\mathrm{Cu}$ [74], and cause additional noise, which can be suppressed only

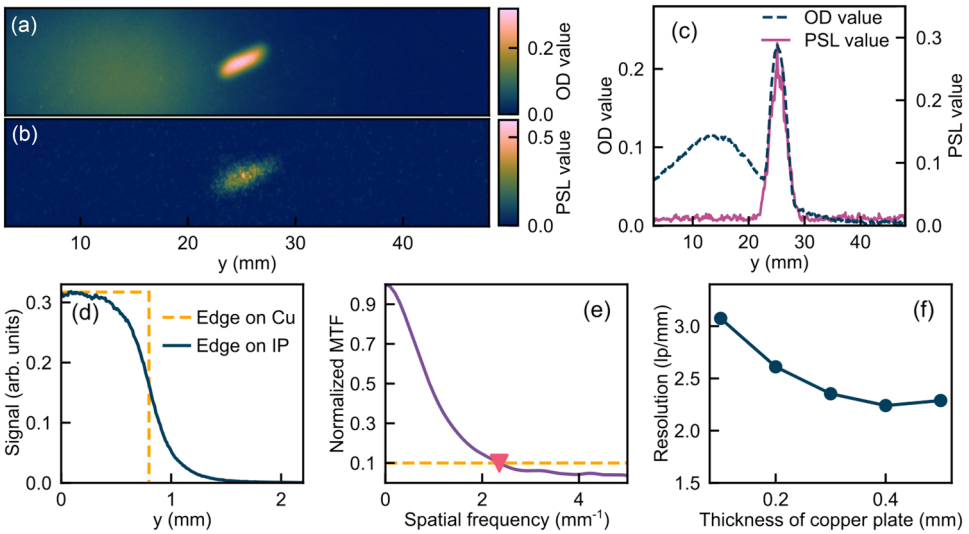

Fig. 5 (Color online) Noise from the electrons and spatial resolution of the radioactivation method. (a) and (b) Distributions of the OD value in EBT-5 and the PSL value in IP-4, respectively, whose central lineouts are plotted in (c). (d) Simulated edge profile on the IP exposed by a 0.3-mm-thick copper plate in FLUKA. A rectangle of size 1 mm × 1.6 mm on the copper plate is radioactivated, while its sharp edge spreads in contact imaging on the IP owing to the scattering of positrons. (e) Corresponding modulation transfer function (MTF) obtained from the Fourier transform of the line spread function, which is calculated by the derivative of the edge profile in (d) [77]. The dashed line corresponds to the MTF value of 0.1, while the intersection is marked by a triangle, whose abscissa represents the maximum distinguishable spatial frequency. (f) Simulated spatial resolution versus the thickness of the copper plate

by using low-Z materials in the stack because the cross-section of the Bremsstrahlung is proportional to Z^2 [75]. The cascaded nuclear reactions, such as ^{65}Cu(p,n)^{65}Zn and ^{63}Cu (n,2n)^{62}Cu, will also influence the radioactivation measurement; these effects have been included in the calculation of P_{ij} in the FLUKA simulations.

Despite the aforementioned advantages, there are also several concerns regarding the radioactivation measurement, one of which is radiation safety as this method is based on nuclear reaction. Based on the proton spectrum shown in Fig. 4d, the yields of ^{63}Zn and ^{62}Cu in the first copper plate are calculated as 4.6×10^6 and 3.9×10^6, respectively. By eliminating the short-lived products, we can estimate the corresponding radioactivity 10 min after the laser shot is 3×10^3 Bq, that is, 0.1 μCi. This radioactivity is lower than that indicated by the standard of Categories-5 radioactive source [76], ensuring the safety of this method. Another concern is its spatial resolution, which is influenced by the scattering of positrons inside the copper plate. We performed a simple FLUKA simulation to investigate how a sharp edge on the copper plate spreads in contact imaging on the IP, as shown in Fig. 5d. A quantitative spatial resolution of 2.4 lp/mm, as displayed in Fig. 5e, can be calculated from the spread profile by using the edge method [77] for a 0.3-mm-thick copper plate. Figure 5f indicates a decrease in the resolution as the plate thickness increases, because a stronger positron scattering occurs in the thicker copper plate. The use of a thinner plate can improve its response R_{ij} and spatial resolution; however, it will reduce the yields of the nuclear reaction products. Hence, we utilized 0.3-mm copper plates for the measurement of the low-energy protons and 0.5-mm plates for the high-energy protons.

Based on the successful demonstration of the spatial and spectral measurements using copper plates in this study, two extensions of the radioactivation method were also investigated, one of which is an online measurement through radioactivation. The current method uses IPs for contact imaging, which must be read by a scanner; this limits the repetition frequency. Real-time imaging can be achieved if a state-of-the-art hybrid semiconductor pixel detector, such as Timepix3 [78] or Mimosa-28 [79] with a spatial resolution of approximately 50 μm, is applied instead of the IP. Simultaneously, the material of the plate should be replaced by elements whose proton-induced reaction product has a half-life of approximately 10 s, because after exposure the plate can be quickly moved to the pixel detector by a linear stage in the vacuum. Aluminum is a promising candidate, whose product from the main reaction channel ^{27}Al(p,n)^{27}Si has a half-life of 4.15 s. Another extension is the achievement of dynamic proton imaging through radioactivation. The principle is to use materials with a narrow peak in the curve of the cross-section depending on the proton energy, such as ^{7}Li and ^{19}F. Hence, the image of each plate corresponds to the signal of the protons in a specific energy range. If a time-varying sample is placed between the proton source and the stack, protons with a higher energy will arrive at the sample

ahead of the low-energy protons [80], subsequently triggering nuclear reactions in a deeper layer of the stack. Thus, the variation of images from different layers can reflect the evolution of the sample in a picosecond time scale. Considering material availability and the half-life of the product, Teflon (C_2F_4) is a suitable candidate, with the main product ^{19}Ne having a half-life of 17.26 s from the reaction $^{19}F(p,n)^{19}Ne$.

5 Conclusion

We demonstrated the simultaneous measurement of the spatial profile and spectrum of laser-accelerated protons through the radioactivation of copper plates, the results of which were sufficiently validated by other methods using RCF and CR-39. The role of positrons, the detection range, influence of electrons, radiation safety, and spatial resolution of this measurement were discussed, revealing the advantages of this method including a high dynamic range and good robustness to electron noise. Two extensions, including an online measurement and dynamic proton imaging, were also proposed to further improve the radioactivation method.

Acknowledgements The authors would like to thank Dr. M. A. Mahmood for the help in unfolding the proton spectrum from the RCF measurement, and Dr. D. Wu for the discussion regarding the proton-induced nuclear reaction.

Author contributions All authors contributed to the study conception and design. Material preparation, data collection and analysis were performed by Yin-Ren Shou, Xue-Zhi Wu and Il Woo Choi. The first draft of the manuscript was written by Yin-Ren Shou. After implementing their comments, all authors approved the final manuscript.

Data availability The data that support the findings of this study are openly available in Science Data Bank at https://doi.org/10.57760/sciencedb.08641 and https://cstr.cn/31253.11.sciencedb.08641.

Conflict of interest The authors declare that they have no competing interests.

References

1. A. Macchi, M. Borghesi, M. Passoni, Ion acceleration by super-intense laser-plasma interaction. Rev. Mod. Phys. **85**, 751–793 (2013). https://doi.org/10.1103/RevModPhys.85.751
2. F. Albert, M. Couprie, A. Debus et al., 2020 roadmap on plasma accelerators. New J. Phys. **23**, 031101 (2021). https://doi.org/10.1088/1367-2630/abcc62
3. B. Dromey, M. Coughlan, L. Senje et al., Picosecond metrology of laser-driven proton bursts. Nat. Commun. **7**, 10642 (2016). https://doi.org/10.1038/ncomms10642
4. T.M. Ostermayr, C. Kreuzer, F.S. Englbrecht et al., Laser-driven X-ray and proton micro-source and application to simultaneous single-shot bi-modal radiographic imaging. Nat. Commun. **11**, 6174 (2020). https://doi.org/10.1038/s41467-020-19838-y
5. J. Bourhis, W.J. Sozzi, P.G. Jorge et al., Treatment of a first patient with FLASH-radiotherapy. Radiother. Oncol. **139**, 18–22 (2019). https://doi.org/10.1016/j.radonc.2019.06.019
6. Y.Q. Yang, W.C. Fang, X.X. Huang et al., Static superconducting gantry-based proton CT combined with X-ray CT as prior image for FLASH proton therapy. Nucl. Sci. Tech. **34**, 11 (2023). https://doi.org/10.1007/s41365-022-01163-2
7. J. Han, Z. Mei, C. Lu et al., Ultra-high dose rate FLASH irradiation induced radio-resistance of normal fibroblast cells can be enhanced by hypoxia and mitochondrial dysfunction resulting from loss of cytochrome C. Front. Cell Dev. Biol. **9**, 672929 (2021). https://doi.org/10.3389/fcell.2021.672929
8. J. Bin, L. Obst-Huebl, J.H. Mao et al., A new platform for ultra-high dose rate radiobiological research using the BELLA PW laser proton beamline. Sci. Rep. **12**, 1484 (2022). https://doi.org/10.1038/s41598-022-05181-3
9. F. Kroll, F.E. Brack, C. Bernert et al., Tumour irradiation in mice with a laser-accelerated proton beam. Nat. Phys. **18**, 316–322 (2022). https://doi.org/10.1038/s41567-022-01520-3
10. J. Zhu, M. Wu, Q. Liao et al., Experimental demonstration of a laser proton accelerator with accurate beam control through image-relaying transport. Phys. Rev. Accel. Beams **22**, 061302 (2019). https://doi.org/10.1103/PhysRevAccelBeams.22.061302
11. P. Bolton, M. Borghesi, C. Brenner et al., Instrumentation for diagnostics and control of laser-accelerated proton (ion) beams. Phys. Med. **30**, 255–270 (2014). https://doi.org/10.1016/j.ejmp.2013.09.002
12. P. Wang, Z. Gong, S.G. Lee et al., Super-heavy ions acceleration driven by ultrashort laser pulses at ultrahigh intensity. Phys. Rev. X **11**, 021049 (2021). https://doi.org/10.1103/PhysRevX.11.021049
13. Y. Shou, D. Kong, P. Wang et al., High-efficiency water-window X-ray generation from nanowire array targets irradiated with femtosecond laser pulses. Opt. Express **29**, 5427–5436 (2021). https://doi.org/10.1364/OE.417512
14. Y. Shou, D. Wang, P. Wang et al., High-efficiency generation of narrowband soft X rays from carbon nanotube foams irradiated by relativistic femtosecond lasers. Opt. Lett. **46**, 3969–3972 (2021). https://doi.org/10.1364/OL.432817
15. Y. Shou, P. Wang, S.G. Lee et al., Brilliant femtosecond-laser-driven hard X-ray flashes from carbon nanotube plasma. Nat. Photon. **17**, 137–142 (2023). https://doi.org/10.1038/s41566-022-01114-8
16. Q. He, K. Ning, R. Lei et al., Spatial and temporal evolution of electromagnetic pulses generated at Shenguang-II series laser facilities. Plasma Sci. Technol **23**, 115202 (2021). https://doi.org/10.1088/2058-6272/ac21b7
17. P. Hu, Z.G. Ma, K. Zhao et al., Development of gated fiber detectors for laser-induced strong electromagnetic pulse environments. Nucl. Sci. Tech. **32**, 58 (2021). https://doi.org/10.1007/s41365-021-00898-8
18. M.A. Mahmood, G.E. Ahn, S.H. Lee et al., Absolute response of a proton detector composed of a microchannel plate assembly and a charge-coupled device to laser-accelerated multi-MeV protons. Rev. Sci. Instrum. **93**, 113311 (2022). https://doi.org/10.1063/5.0118775
19. P. Varmazyar, P.K. Singh, Z. Elekes et al., Calibration of microchannel plate detector in a Thomson spectrometer for protons and carbon ions with energies below 1 MeV. Rev. Sci. Instrum. **93**, 073301 (2022). https://doi.org/10.1063/5.0086747
20. H. Sakaki, M. Kanasaki, Y. Fukuda et al., Development of a single-shot-imaging thin film for an online Thomson parabola spectrometer. Rev. Sci. Instrum. **84**, 013301 (2013). https://doi.org/10.1063/1.4773546
21. M. Salvadori, F. Consoli, C. Verona et al., Accurate spectra for high energy ions by advanced time-of-flight

diamond-detector schemes in experiments with high energy and intensity lasers. Sci. Rep. **11**, 3071 (2021). https://doi.org/10.1038/s41598-021-82655-w
22. Y. Zhang, Z. Zhang, B. Zhu et al., An angular-resolved multi-channel Thomson parabola spectrometer for laser-driven ion measurement. Rev. Sci. Instrum. **89**, 093302 (2018). https://doi.org/10.1063/1.5042424
23. S. Kojima, S. Inoue, T.H. Dinh et al., Compact Thomson parabola spectrometer with variability of energy range and measurability of angular distribution for low-energy laser-driven accelerated ions. Rev. Sci. Instrum. **91**, 053305 (2020). https://doi.org/10.1063/5.0005450
24. C. Salgado-López, J.I. Apiñaniz, J.L. Henares et al., Angular-resolved Thomson parabola spectrometer for laser-driven ion accelerators. Sensors **22**, 3239 (2022). https://doi.org/10.3390/s22093239
25. D. Jung, R. Hörlein, D.C. Gautier et al., A novel high resolution ion wide angle spectrometer. Rev. Sci. Instrum. **82**, 043301 (2011). https://doi.org/10.1063/1.3575581
26. Y. Zheng, L.N. Su, M. Liu et al., Note: A new angle-resolved proton energy spectrometer. Rev. Sci. Instrum. **84**, 096103 (2013). https://doi.org/10.1063/1.4820918
27. S. Yang, Y. Deng, X. Ge et al., A two-dimensional wide-angle proton spectrometer with improved angular resolution. Nucl. Instrum. Meth. A **860**, 29–34 (2017). https://doi.org/10.1016/j.nima.2017.03.063
28. W. Wang, X.X. Yuan, X.H. Cai, A beam range monitor based on scintillator and multi-pixel photon counter arrays for heavy ions therapy. Nucl. Sci. Tech. **33**, 123 (2022). https://doi.org/10.1007/s41365-022-01113-y
29. J. Metzkes, K. Zeil, S. Kraft et al., An online, energy-resolving beam profile detector for laser-driven proton beams. Rev. Sci. Instrum. **87**, 083310 (2016). https://doi.org/10.1063/1.4961576
30. N. Dover, M. Nishiuchi, H. Sakaki et al., Scintillator-based transverse proton beam profiler for laser-plasma ion sources. Rev. Sci. Instrum. **88**, 073304 (2017). https://doi.org/10.1063/1.4994732
31. M. Hesse, T. Ebert, M. Zimmer et al., Spatially resolved online particle detector using scintillators for laser-driven particle sources. Rev. Sci. Instrum. **92**, 093302 (2021). https://doi.org/10.1063/5.0052507
32. D. Mariscal, B. Djordjević, R. Anirudh et al., A flexible proton beam imaging energy spectrometer (PROBIES) for high repetition rate or single-shot high energy density (HED) experiments. Rev. Sci. Instrum. **94**, 023507 (2023). https://doi.org/10.1063/5.0101845
33. J. Metzkes, L. Karsch, S. Kraft et al., A scintillator-based online detector for the angularly resolved measurement of laser-accelerated proton spectra. Rev. Sci. Instrum. **83**, 123301 (2012). https://doi.org/10.1063/1.4768672
34. M. Huault, D. De Luis, J. Apiñaniz et al., A 2D scintillator-based proton detector for high repetition rate experiments. High Power Laser Sci. Eng. **7**, e60 (2019). https://doi.org/10.1017/hpl.2019.43
35. J. Green, M. Borghesi, C. Brenner et al., in Laser acceleration of electrons, protons, and ions; and medical applications of laser-generated secondary sources of radiation and particles, vol. 8079 , pp. 147–154. SPIE, (2011). https://doi.org/10.1117/12.888967
36. D. Golovin, S. Mirfayzi, S. Shokita et al., Calibration of imaging plates sensitivity to high energy photons and ions for laser-plasma interaction sources. J. Instrum. **16**, T02005 (2021). https://doi.org/10.1088/1748-0221/16/02/T02005
37. M.E. Howard, M.G. Herman, M.P. Grams, Methodology for radiochromic film analysis using FilmQA Pro and ImageJ. PLoS ONE **15**, e0233562 (2020). https://doi.org/10.1371/journal.pone.0233562
38. Y. Zhang, L.X. Liu, H.W. Wang et al., Primary yields of protons measured using CR-39 in laser-induced deuteron-deuteron fusion reactions. Nucl. Sci. Tech. **31**, 62 (2020). https://doi.org/10.1007/s41365-020-00769-8
39. S. Gaillard, J. Fuchs, N. Renard-Le Galloudec et al., Study of saturation of CR39 nuclear track detectors at high ion fluence and of associated artifact patterns. Rev. Sci. Instrum. **78**, 013304 (2007). https://doi.org/10.1063/1.2400020
40. F. Wagner, O. Deppert, C. Brabetz et al., Maximum proton energy above 85 MeV from the relativistic interaction of laser pulses with micrometer thick CH_2 targets. Phys. Rev. Lett. **116**, 205002 (2016). https://doi.org/10.1103/PhysRevLett.116.205002
41. A. Higginson, R. Gray, M. King et al., Near-100 MeV protons via a laser-driven transparency-enhanced hybrid acceleration scheme. Nat. Commun. **9**, 724 (2018). https://doi.org/10.1038/s41467-018-03063-9
42. I. Spencer, K. Ledingham, R. Singhal et al., Laser generation of proton beams for the production of short-lived positron emitting radioisotopes. Nucl. Instrum. Meth. B **183**, 449–458 (2001). https://doi.org/10.1016/S0168-583X(01)00771-6
43. M.I.K. Santala, M. Zepf, F.N. Beg et al., Production of radioactive nuclides by energetic protons generated from intense laser-plasma interactions. Appl. Phys. Lett. **78**, 19–21 (2001). https://doi.org/10.1063/1.1335849
44. M. Tarisien, C. Plaisir, F. Gobet et al., NATALIE: A 32 detector integrated acquisition system to characterize laser produced energetic particles with nuclear techniques. Rev. Sci. Instrum. **82**, 023302 (2011). https://doi.org/10.1063/1.3527061
45. L. Willingale, S.R. Nagel, A.G.R. Thomas et al., Characterization of laser-driven proton beams from near-critical density targets using copper activation. J. Plasma Phys. **81**, 365810102 (2014). https://doi.org/10.1017/s002237781400066x
46. J. Yang, P. McKenna, K. Ledingham et al., Nuclear reactions in copper induced by protons from a petawatt laser-foil interaction. Appl. Phys. Lett. **84**, 675–677 (2004). https://doi.org/10.1063/1.1645314
47. R. Clarke, P. Simpson, S. Kar et al., Nuclear activation as a high dynamic range diagnostic of laser-plasma interactions. Nucl. Instrum. Meth. A **585**, 117–120 (2008). https://doi.org/10.1016/j.nima.2007.11.015
48. M.M. Günther, A. Britz, R.J. Clarke et al., NAIS: nuclear activation-based imaging spectroscopy. Rev. Sci. Instrum. **84**, 073305 (2013). https://doi.org/10.1063/1.4815826
49. S.K. He, D.X. Liu, J.L. Jiao et al., Charged paricle activation analysis for characterizing parameters of laser-accelerated protons. Acta Phys. Sin. **66**, 075203 (2017). https://doi.org/10.7498/aps.66.205201
50. G. Battistoni, T. Boehlen, F. Cerutti et al., Overview of the FLUKA code. Ann. Nucl. Energy **82**, 10–18 (2015). https://doi.org/10.1016/j.anucene.2014.11.007
51. I.W. Choi, C. Jeon, S.G. Lee et al., Highly efficient double plasma mirror producing ultrahigh-contrast multi-petawatt laser pulses. Opt. Lett. **45**, 6342–6345 (2020). https://doi.org/10.1364/OL.409749
52. J.F. Ziegler, M. Ziegler, J. Biersack, SRIM-the stopping and range of ions in matter (2010). Nucl. Instrum. Meth. B **268**, 1818–1823 (2010). https://doi.org/10.1016/j.nimb.2010.02.091
53. P. Casolaro, Radiochromic films for the two-dimensional dose distribution assessment. Appl. Sci. **11**, 2132 (2021). https://doi.org/10.3390/app11052132
54. I. Choi, H. Kim, N. Hafz et al., Target diagnostic systems for proton, electron, and X-ray generation experiments based on ultraintense laser-target interactions. J. Korean Phys. Soc. **55**, 517–527 (2009). https://doi.org/10.3938/jkps.55.517

55. S. Devic, N. Tomic, D. Lewis, Reference radiochromic film dosimetry: review of technical aspects. Phys. Med. **32**, 541–556 (2016). https://doi.org/10.1016/j.ejmp.2016.02.008
56. Y.F. He, X.F. Xi, S.L. Guo et al., Calibration of CR-39 solid-state track detectors for study of laser-driven nuclear reactions. Nucl. Sci. Tech. **31**, 42 (2020). https://doi.org/10.1007/s41365-020-0749-1
57. C.A. Schneider, W.S. Rasband, K.W. Eliceiri, NIH Image to ImageJ: 25 years of image analysis. Nat. Meth. **9**, 671–675 (2012). https://doi.org/10.1038/nmeth.2089
58. M. Kanasaki, T. Yamauchi, K. Oda et al., in Progress in ultrafast intense laser science XV , pp. 133–147. Springer (2020). https://doi.org/10.1007/978-3-030-47098-2_7
59. D. Nikezic, M. Ivanovic, K. Yu, A computer program TRACK_P for studying proton tracks in PADC detectors. SoftwareX **5**, 74–79 (2016). https://doi.org/10.1016/j.softx.2016.04.006
60. Y. Zhang, H.W. Wang, Y.G. Ma et al., Energy calibration of a CR-39 nuclear-track detector irradiated by charged particles. Nucl. Sci. Tech. **30**, 87 (2019). https://doi.org/10.1007/s41365-019-0619-x
61. T.W. Jeong, P. Singh, C. Scullion et al., CR-39 track detector for multi-MeV ion spectroscopy. Sci. Rep. **7**, 2152 (2017). https://doi.org/10.1038/s41598-017-02331-w
62. C. Ahdida, D. Bozzato, D. Calzolari et al., New capabilities of the FLUKA multi-purpose code. Front. Phys. **9**, 788253 (2022). https://doi.org/10.3389/fphy.2021.788253
63. G. Boutoux, N. Rabhi, D. Batani et al., Study of imaging plate detector sensitivity to 5–18 MeV electrons. Rev. Sci. Instrum. **86**, 113304 (2015). https://doi.org/10.1063/1.4936141
64. G. Boutoux, D. Batani, F. Burgy et al., Validation of modelled imaging plates sensitivity to 1–100 keV x-rays and spatial resolution characterisation for diagnostics for the PETawatt Aquitaine Laser. Rev. Sci. Instrum. **87**, 043108 (2016). https://doi.org/10.1063/1.4944863
65. Scikit-opt. https://github.com/guofei9987/scikit-opt (2023)
66. B. Maddox, H. Park, B. Remington et al., High-energy X-ray backlighter spectrum measurements using calibrated image plates. Rev. Sci. Instrum. **82**, 023111 (2011). https://doi.org/10.1063/1.3531979
67. G.J. Williams, B.R. Maddox, H. Chen et al., Calibration and equivalency analysis of image plate scanners. Rev. Sci. Instrum. **85**, 11E604 (2014). https://doi.org/10.1063/1.4886390
68. X. Xu, Q. Liao, M. Wu et al., Detection and analysis of laser driven proton beams by calibrated Gafchromic HD-V2 and MD-V3 radiochromic films. Rev. Sci. Instrum. **90**, 033306 (2019). https://doi.org/10.1063/1.5049499
69. R. Castriconi, M. Ciocca, A. Mirandola et al., Dose-response of EBT3 radiochromic films to proton and carbon ion clinical beams. Phys. Med. Biol. **62**, 377 (2016). https://doi.org/10.1088/1361-6560/aa5078
70. M.A. Mahmood, S.G. Lee, S.H. Lee et al., Calibration of radiochromic EBT3 film using laser-accelerated protons. Rev. Sci. Instrum. **92**, 023302 (2021). https://doi.org/10.1063/5.0031253
71. F. Kondev, M. Wang, W. Huang et al., The NUBASE2020 evaluation of nuclear physics properties. Chin. Phys. C **45**, 030001 (2021). https://doi.org/10.1088/1674-1137/abddae
72. T. Bonnet, M. Comet, D. Denis-Petit et al., Response functions of imaging plates to photons, electrons and He particles. Rev. Sci. Instrum. **84**, 103510 (2013). https://doi.org/10.1063/1.4826084
73. M. Berger, J. Coursey, M. Zucker et al., Stopping-power & range tables for electrons, protons, and helium ions. NIST Standard Reference Database p. 124 (2017). https://doi.org/10.18434/T4NC7P
74. S. Reed, V. Chvykov, G. Kalintchenko et al., Efficient initiation of photonuclear reactions using quasimonoenergetic electron beams from laser wakefield acceleration. J. Appl. Phys. **102**, 073103 (2007). https://doi.org/10.1063/1.2787159
75. J. Galy, M. Maučec, D. Hamilton et al., Bremsstrahlung production with high-intensity laser matter interactions and applications. New J. Phys. **9**, 23 (2007). https://doi.org/10.1088/1367-2630/9/2/023
76. Categorization of Radioactive Sources. No. RS-G-1.9 in General Safety Guides (International Atomic Energy Agency, Vienna, 2005). https://www.iaea.org/publications/7237/categorization-of-radioactive-sources
77. F. Viallefont-Robinet, D. Helder, R. Fraisse et al., Comparison of MTF measurements using edge method: towards reference data set. Opt. Express **26**, 33625–33648 (2018). https://doi.org/10.1364/OE.26.033625
78. P. Rubovič, A. Bonasera, P. Burian et al., Measurements of D-D fusion neutrons generated in nanowire array laser plasma using Timepix3 detector. Nucl. Instrum. Meth. A **985**, 164680 (2021). https://doi.org/10.1016/j.nima.2020.164680
79. T.N. Pham, P. Marchand, C. Finck et al., ^{18}F autoradiography with the Mimosa-28: characterization and application. IEEE Trans. Radiat. Plasma Med. Sci. **4**, 630–636 (2020). https://doi.org/10.1109/TRPMS.2020.2996912
80. M. Borghesi, D. Campbell, A. Schiavi et al., Electric field detection in laser-plasma interaction experiments via the proton imaging technique. Phys. Plasmas **9**, 2214–2220 (2002). https://doi.org/10.1063/1.1459457